AFRL-RY-WP-TR-2021-0063

OPTICAL PHASED ARRAYS WITH SUB-WAVELENGTH ELEMENT SIZE AND SPACING (OPA-SWESS)

Firooz Aflatouni
University of Pennsylvania

JUNE 2021
Final Report

STINFO COPY

AIR FORCE RESEARCH LABORATORY
SENSORS DIRECTORATE
WRIGHT-PATTERSON AIR FORCE BASE, OH 45433-7320
AIR FORCE MATERIEL COMMAND
UNITED STATES AIR FORCE

NOTICE AND SIGNATURE PAGE

Using Government drawings, specifications, or other data included in this document for any purpose other than Government procurement does not in any way obligate the U.S. Government. The fact that the Government formulated or supplied the drawings, specifications, or other data does not license the holder or any other person or corporation; or convey any rights or permission to manufacture, use, or sell any patented invention that may relate to them.

This report is the result of contracted fundamental research deemed exempt from public affairs security and policy review in accordance with SAF/AQR memorandum dated 10 Dec 08 and AFRL/CA policy clarification memorandum dated 16 Jan 09. This report is available to the general public, including foreign nationals.

Copies may be obtained from the Defense Technical Information Center (DTIC) (http://www.dtic.mil).

AFRL-RY-WP-TR-2021-0063 HAS BEEN REVIEWED AND IS APPROVED FOR PUBLICATION IN ACCORDANCE WITH ASSIGNED DISTRIBUTION STATEMENT.

USECHAK.NICHOLAS.G.1300868700
Digitally signed by USECHAK.NICHOLAS.G.1300868700
Date: 2021.06.11 09:37:44 -04'00'

NICHOLAS G. USECHAK
Program Manager
Highly Integrated Microsystems Branch
Aerospace Components & Subsystems Division

HARY.STEPHEN.L.1230193416
Digitally signed by HARY.STEPHEN.L.1230193416
Date: 2021.06.11 11:30:48 -04'00'

STEPHEN L. HARY, Chief
Highly Integrated Microsystems Branch
Aerospace Components & Subsystems Division

ARNOLD.FRED.E.1230167598
Digitally signed by ARNOLD.FRED.E.1230167598
Date: 2021.06.11 13:08:42 -04'00'

FRED E. ARNOLD
Deputy (Acting)
Aerospace Components & Subsystems Division
Sensors Directorate

This report is published in the interest of scientific and technical information exchange and its publication does not constitute the Government's approval or disapproval of its ideas or findings.

REPORT DOCUMENTATION PAGE

Form Approved
OMB No. 0704-0188

1. REPORT DATE *(DD-MM-YY)*	2. REPORT TYPE	3. DATES COVERED *(From - To)*
June 2021	Final	6 March 2018 – 6 September 2020

4. TITLE AND SUBTITLE
OPTICAL PHASED ARRAYS WITH SUB-WAVELENGTH ELEMENT SIZE AND SPACING (OPA-SWESS)

5a. CONTRACT NUMBER
FA8650-18-1-7828

5b. GRANT NUMBER

5c. PROGRAM ELEMENT NUMBER
62716E

6. AUTHOR(S)
Firooz Aflatouni

5d. PROJECT NUMBER
N/A

5e. TASK NUMBER
N/A

5f. WORK UNIT NUMBER
Y1RV

7. PERFORMING ORGANIZATION NAME(S) AND ADDRESS(ES)
University of Pennsylvania
3451 Walnut St
Philadelphia, PA 19104-6205

8. PERFORMING ORGANIZATION REPORT NUMBER

9. SPONSORING/MONITORING AGENCY NAME(S) AND ADDRESS(ES)
Air Force Research Laboratory
Sensors Directorate
Wright-Patterson Air Force Base, OH 45433-7320
Air Force Materiel Command
United States Air Force

Defense Advanced Research Projects Agency (DARPA)
675 North Randolph Street
Arlington, VA 22203

10. SPONSORING/MONITORING AGENCY ACRONYM(S)
AFRL/RYDI

11. SPONSORING/MONITORING AGENCY REPORT NUMBER(S)
AFRL-RY-WP-TR-2021-0063

12. DISTRIBUTION/AVAILABILITY STATEMENT
DISTRIBUTION STATEMENT A. Approved for public release; distribution is unlimited.

13. SUPPLEMENTARY NOTES
This report is the result of contracted fundamental research deemed exempt from public affairs security and policy review in accordance with The Under Secretary of Defense memorandum dated 24 May 2010. This material is based on research sponsored by the Defense Advanced Research Projects Agency (DARPA) and contracted by the Air Force Research Lab (AFRL) under agreement number FA8650-18-1-7828. The U.S. Government is authorized to reproduce and distribute reprints for Governmental purposes notwithstanding any copyright notation thereon. The views and conclusions contained herein are those of the authors and should not be interpreted as necessarily representing the official policies or endorsements, either expressed or implied, of AFRL, DARPA or the U.S. Government. Report contains color.

14. ABSTRACT
This program sought to develop the technologies necessary to demonstrate planar, millimeter-scale, transmit and receive, non-mechanical beam steering optical phased arrays. The objective was to develop optical-array-element integrated photonic circuit unit cells with high fill-factor apertures. These cells should be amenable to scaling, thus enabling the assembly of larger higher-power coherent apertures. The scope of this effort is to advance integrated phase shifters in a silicon photonics unit cell component to improve on the performance of the bulk photonic devices currently used in optical beamforming systems.

15. SUBJECT TERMS
OPA, integrated photonics, LiDAR

16. SECURITY CLASSIFICATION OF:			17. LIMITATION OF ABSTRACT:	18. NUMBER OF PAGES	19a. NAME OF RESPONSIBLE PERSON (Monitor)
a. REPORT	b. ABSTRACT	c. THIS PAGE			Nicholas Usechak
Unclassified	Unclassified	Unclassified	SAR	33	19b. TELEPHONE NUMBER *(Include Area Code)* N/A

Table of Contents

Section **Page**

List of Figures

Figure **Page**

1 SUMMARY

An important feature of microwave phased arrays is the sub-wavelength spacing between the emitting elements which can eliminate the side-lobes. Despite significant advancements in the design and implementation of optical phased arrays (OPAs), no OPA with sub-wavelength element size and spacing has been demonstrated to the best of our knowledge. For such designs, the optical phase shifters must be ultra-compact while immune to cross-talk. Also, the sub-wavelength spacing between the emitters make the optical routing challenging. Another significant challenge is electrical routing for optical element control. For sub-wavelength element spacing, the metal layers can cause optical loss while suffering from electro-migration (current handling) limitations. Also, state-of-the-art through-silicon vias (TSVs) are significantly larger than the array elements and their pitch and are therefore not helpful when it comes to electrical routing. In this program we proposed two methods to demonstrate **Optical Phased Arrays with Sub-Wavelength Element Size and Spacing (OPA-SWESS)** at 1550 nm. In both methods, sub-wavelength emitter size and spacing could be realized though utilizing three dimensional (3-D) structures and techniques, where the array element size and pitch is set independent of the size of the optical phase shifters.

In method 1 a multi-layer photonic system is used to adjust the phase and amplitude of the optical signals outside the array aperture on row and column waveguides (formed on different layers), routed to the array on the same layer, and combined at each element. In this case, the relative phase between elements in the rows and columns of the array can be adjusted by setting the amplitude and phase of optical waves guided to the aperture.

In method 2 an array of vertical phase shifters made of doped silicon pillars placed on top of a two dimensional (2-D) array of grating couplers with sub-wavelength size and spacing was proposed to be implemented to form a 2-D OPA. Use of silicon pillars as phase shifters not only allows for much more compact placement of emitters, but also significantly reduces the undesired wavelength dependent steering caused by the grating couplers.

2 INTRODUCTION

2.1 Background

An OPA is an array of optical emitting or receiving antennas (elements) that enables beam-forming and steering and is widely used in various applications including optical communications [1], LiDAR systems [2-4], projection systems [5], and 3-D imaging [6]. In such systems, the far-field beam is formed and steered by controlling the relative phases between optical elements within the array aperture. Benefiting from integrated photonic platforms, a number of OPAs have been demonstrated [2-15]. In the conventional implementation of a 2-D NxN element OPA, N^2 phase shifters are used to perform per-element optical phase adjustment [2-5,7,8].

To form a narrow beam with a large side-lobe suppression ratio, which is steerable over a large field-of-view, a large number of closely placed elements (ideally with element spacing approaching half of the wavelength) within a large aperture is required. This results in a large power consumption in a conventional 2-D OPA with per-element phase shifters and makes the optical and electrical routing within the array aperture rather challenging.

In OPAs with grating based elements (*e.g.* grating couplers), this challenge can be addressed by steering the beam in one dimension through adjusting the relative phases between the elements, while changing the optical wavelength for beam-steering in the other dimension [12-15]. Despite excellent beam-steering results, this method requires a highly tunable laser (over a large wavelength range) and typically achieves a smaller steering range through wavelength tuning compared to the relative phase adjustment between the OPA elements. Such OPAs are essentially 1-D OPAs and are not generally compatible with applications such as OPA-based optical communication.

Despite significant advancements in the design and implementation of OPAs, no OPA with sub-wavelength element size and spacing has been demonstrated to the best of our knowledge. For such designs, the optical phase shifters must be ultra-compact and immune to cross-talk. Moreover, the sub-wavelength spacing between the emitters makes the optical routing challenging. Another significant challenge is electrical routing for optical element control. For sub-wavelength element spacing, the metal layers can cause optical loss while suffering from electro-migration (current handling) limitations. State-of-the-art through-silicon vias (TSVs) are also significantly larger than the array elements and their pitch and are therefore not helpful when it comes to electrical routing for this application.

2.2 Approach

In this program, we proposed two methods to demonstrate **Optical Phased Arrays with Sub-Wavelength Element Size and Spacing** at 1550 nm**.** In both methods, sub-wavelength emitter size and spacing is realized though utilizing 3D structures and techniques, where the array element size and pitch is set independent of the size of the optical phase shifters. In method 1, we introduced novel OPA architectures, where for 2-D beam-steering in an NxN OPA, only 2N phase shifters outside of the array aperture are used to adjust the relative phases

between elements and no laser wavelength tuning is required. In the proposed schemes, the number of phase shifters for an NxN array is reduced from N^2 (for a conventional 2-D OPA) to 2N, significantly reducing the power consumption of an OPA with a large number of elements. Furthermore, placing the phase shifters outside of the array aperture enables realization of OPAs with compact element spacing and eliminates the electrical routing within the aperture and the corresponding metal induced optical loss. In a modified design, the element spacing is further reduced though the implementation of multi-layer tilted antennas in a 2-layer silicon photonics process.

In method 2, an array of vertical phase shifters made of lightly doped silicon pillars placed on top of a 2D array of grating couplers with sub-wavelength size and spacing. A single optical waveguide is used as the feed line for each row and different tap couplers are designed to couple the light into each emitter in a row. The coupling ratios are designed to ensure the same power is radiated from each emitter. The use of silicon pillars as phase shifters not only allows for a more compact placement of the emitters, but also significantly reduces the undesired wavelength dependent steering caused by the grating couplers making such a system compatible with many applications including free-space optical communications.

2.3 Scope

In method 1 we have implemented two 8x8 OPAs. Figure 1(a) shows the structure of the 8x8 OPA which uses 16 phase shifters to perform 2-D beam-steering without any need to adjust the optical wavelength. Using the aperture size of 77 μm x 77 μm for the OPA transmitter, far-field beam steering over a range of about 7° is demonstrated. Figure 1(b) shows the microphotograph of the 8x8 multi-layer 2-D OPA. In this case a beam is formed through the near-field interference between superimposed waves emitted from array elements on each layer. Vertically aligned tilted scatterers, 3-D optical signal distribution and processing, and off-aperture phase control enable the realization of an element-pitch of 3 μm. The 64-element 2-D OPA achieves a steering range of 23° using only 16 phase shifters.

In method 2 we have implemented 16x16, 32x32, and 64x64 OPAs with silicon pillars. Figure 1(c) shows the top view of the 32x32 OPA. We have demonstrated 1D beam-steering though wavelength tuning but, due to COVID-19 restrictions, have not been able to demonstrated 2D beam-steering yet.

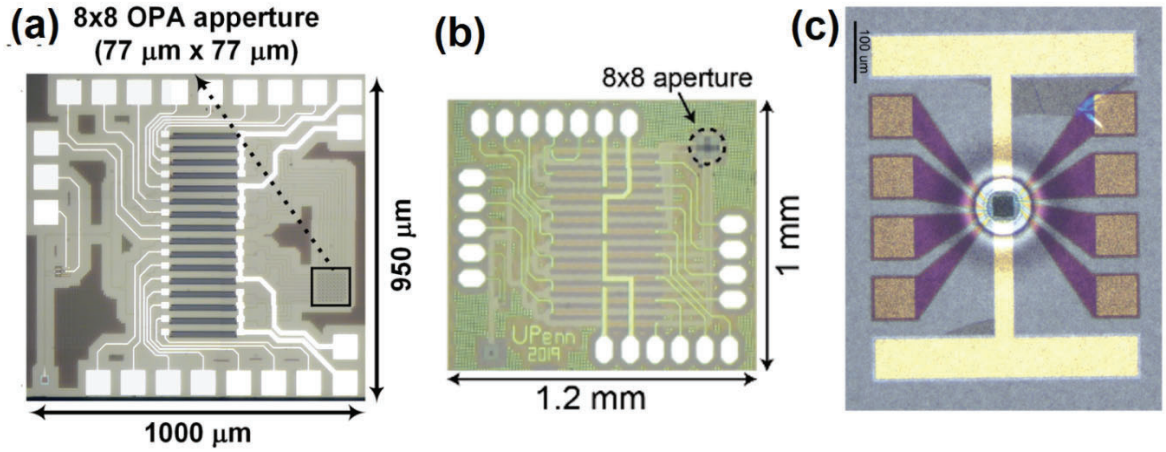

Figure 1: Implemented Systems under this Program

The implemented 8x8 OPA with remote phase adjustment (a) The implemented multi-layer 8x8 OPA (b) and (c) The OPA with silicon pillars as emitting elements.

3 METHODS, ASSUMPTIONS, AND PROCEDURES

3.1 OPA Theory of Operation

In an OPA the beam forming and steering is performed by controlling the relative phases between elements. Figure 2(a) shows the structure of the proposed NxN OPA, where N nanophotonic waveguides serving as rows cross N nanophotonic waveguides serving as columns.

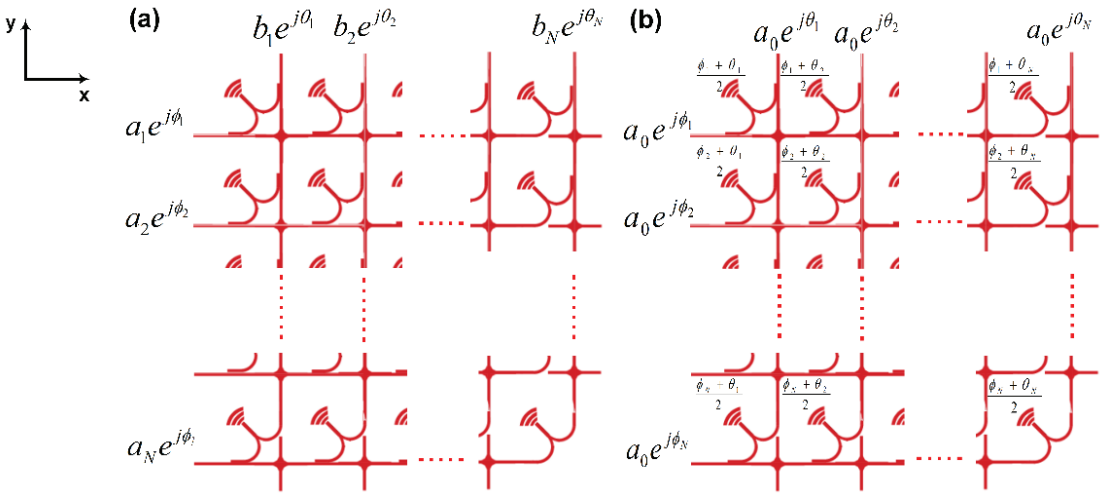

Figure 2: Conceptual Schematic of the Proposed NxN OPA
Optical signals traveling in the row and column waveguides have (a) different phases and amplitudes and (b) different phases but the same amplitude.

Consider the case where the electric field of optical wave entering the m^{th} row is written as $E_m = a_m e^{j\phi_m}$, and the electric field of optical wave entering the n^{th} column is written as $E_n = b_n e^{j\theta_n}$ where a_m, b_n, ϕ_m, and θ_n are the amplitude of the optical field in the m^{th} row, the amplitude of the optical field in the n^{th} column, the phase of the optical signal in the m^{th} row, and the phase of the optical signal in the n^{th} column, respectively. Note that the term $e^{j\omega_0 t}$, representing the optical frequency of the signal, is dropped for simplicity. Before the crossing point of the m^{th} row and the n^{th} column, two directional couplers with varying coupling ratio followed by a Y-junction are used to combine a fraction of the light from the m^{th} row with a fraction of the light from the n^{th} column. The Y-junction output is connected to a grating coupler, GC_{mn}, acting as the OPA element. The length of each directional coupler as well as the etch level in the coupling region is adjusted to ensure all grating couplers receive the same power. The electric field at the input of GC_{mn} is written as

$$E_{mn} = \frac{1}{\sqrt{N}}\sqrt{\left(a_m^2 + b_n^2 + 2a_m b_n \cos(\phi_m - \theta_n)\right)}\exp\left[j\tan^{-1}\left(\frac{a_m \sin\phi_m + b_n \sin\theta_n}{a_m \cos\phi_m + b_n \cos\theta_n}\right)\right]. \quad (1)$$

In this case, the relative phase between GC_{mn} and $GC_{(\text{m+1})\text{n}}$ can be written as

$$\Delta\phi_{m+1,m,n} = \tan^{-1}\left(\frac{a_{m+1}\sin\phi_{m+1} + b_n \sin\theta_n}{a_{m+1}\cos\phi_{m+1} + b_n \cos\theta_n}\right) - \tan^{-1}\left(\frac{a_m \sin\phi_m + b_n \sin\theta_n}{a_m \cos\phi_m + b_n \cos\theta_n}\right). \quad (2)$$

Similarly, the relative phase between GC_{mn} and $GC_{m(n+1)}$ can be written as

$$\Delta\theta_{m,n+1,n} = \tan^{-1}\left(\frac{a_m \sin\phi_m + b_{n+1}\sin\theta_{n+1}}{a_m \cos\phi_m + b_{n+1}\cos\theta_{n+1}}\right) - \tan^{-1}\left(\frac{a_m \sin\phi_m + b_n \sin\theta_n}{a_m \cos\phi_m + b_n \cos\theta_n}\right). \quad (3)$$

Equations (2) and (3) indicate that the relative phase between adjacent elements can be set by adjusting the amplitude and phase of the optical waves in the row and column waveguides outside the aperture. Note one potential drawback (e.g. for seeking to improve beam propagation through turbulence) is that the phase of the individual element cannot be independently set. However, the relative phase between the adjacent elements in the X and Y directions (in Figure 2(a) and 2(b)) can be set to any value between 0 and 2π radians, enabling formation of a beam that can be steered in X and Y directions independently. For the case when $a_m = b_n = a_0$ (Fig. 2(b)), Eq. (1) can be simplified as

$$E_{mn} = \frac{2}{\sqrt{N}} a_0 \left|\cos\left(\frac{\phi_m - \theta_n}{2}\right)\right| e^{j\left(\frac{\phi_m + \theta_n}{2}\right)}. \quad (4)$$

In this case, the relative phase between the adjacent elements in rows and columns can be written as $\Delta\phi_{m+1,m,n} = \frac{\phi_{m+1} - \phi_m}{2}$ and $\Delta\theta_{m,n+1,n} = \frac{\theta_{n+1} - \theta_n}{2}$, respectively. In order to perform 2-D beam-steering, the relative phase between all adjacent elements in rows is set to the same value, *i.e.* $\Delta\phi_{m+1,m,n} = \Delta\phi$ and, similarly, the relative phase between all adjacent elements in columns is set to $\Delta\theta_{m,n+1,n} = \Delta\theta$. Therefore, 2N phase shifters can be used to perform 2-D beam-steering for an NxN OPA, which significantly reduces the power consumption for an OPA with a large number of elements, while also eliminating the electrical routing within the aperture. Furthermore, moving the phase shifters outside of the aperture enables smaller element spacing for a 2-D phase array.

In Eq. (4), the amplitude of the electric field at GC_{mn} is proportional to the term $\left|\cos\left((\phi_m - \theta_n)/2\right)\right|$. Therefore, the light emission intensity from the grating couplers may be lower than that from conventional 2-D OPAs, where per-element phase shifters (with low phase dependent insertion loss) are used. To study the performance of the proposed 2-D OPA and also investigate the effect of the aforementioned phase dependent amplitude variation on the beam forming and steering, the Fraunhofer far-field approximation [16] is used to calculate the far-field interference pattern of an 8x8 OPA implemented based on the proposed architecture (with 16 off-aperture phase shifters), which is compared with that of a conventional 8x8 OPA with 64 per-element phase shifters in Fig. 3(a) for the case of diagonal beam-steering. The two OPAs have identical element structure with the same element spacing of 11 μm. The diagonal beam-steering is performed by setting the same relative phase of 0, 30°, 60°, 120°, and 180° between the adjacent elements in both rows and columns. The normalized main-lobe power for the different steering angles of these two 8x8 OPAs is compared in Fig. 3(b). As predicted by Eq. (4), the intensity of the main lobe for the proposed OPA is generally lower than that of the conventional OPA. Note

that in Fig. 3(a), for a relative phase of 180° between the adjacent elements in the proposed OPA, the intensity of every other element is zero (caused by the cosine term in Eq. (4)), effectively doubling the OPA element spacing, which results in a factor of 2 smaller lobe-spacing.

The side-lobe suppression ratio was calculated using the simulated far-field pattern in Fig. 3(a). In the conventional OPA with per-element phase control, a the side-lobe suppression ratio of about 13 dB is calculated, which is reduced to about 9 dB for the proposed OPA with off-aperture phase adjustment due to the phase dependent amplitude effect described by Eq. (4). Note that the proposed architecture here can be used to form and steer a single beam. However, unlike 2D OPAs with per-element phase shifters, it is not capable of multi-beam forming and steering.

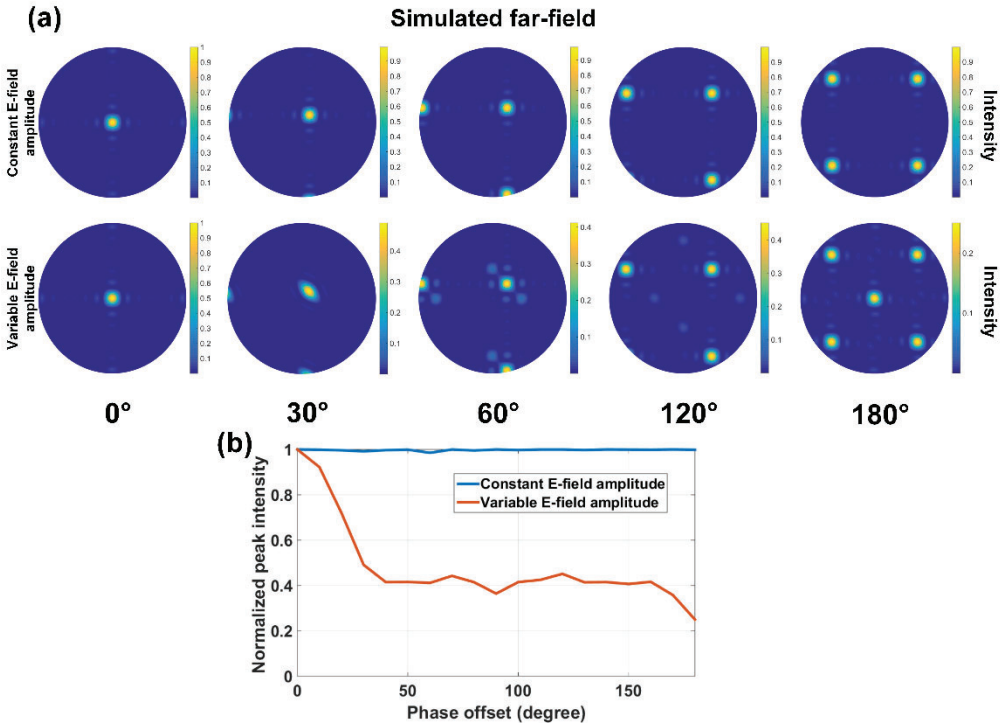

Figure 3: The Far-field Interference Pattern of an 8x8 OPA

64 per-element phase control (top row) and that of an 8x8 OPA with identical element structure and spacing but implemented based on the proposed architecture (bottom row). The diagonal beam-steering (with same relative phase between the elements in rows and columns) is performed (a). The peak intensity of the main lobe in the far-field pattern for the conventional and proposed 8x8 OPAs (b).

3.2 Single-Layer OPA System Design

Figures 4(a) and 4(b) show the structure of the implemented OPA transmitter. The input light is coupled into the chip using an on-chip grating coupler and is guided to a network of Y-junction splitters. The splitter network uniformly splits the coupled light into 16 branches. The phase of optical wave in the nanophotonic waveguide in each branch is adjusted through a thermal phase shifter. After phase adjustment, 8 nanophotonic waveguides serving as rows and 8 nanophotonic waveguides serving as columns are used to guide the optical waves to an array of 8x8 grating

couplers serving as the OPA elements. Each grating coupler is placed near the crossing point of a row and a column waveguide and is fed by two directional couplers followed by a Y-junction combiner used to combine a fraction of the light from the corresponding row and column waveguides. The directional couplers have varying lengths to ensure that all grating couplers receive the same optical power. The spacing between the grating couplers within the array aperture is 11 μm and they are placed symmetrically with respect to the row and column waveguides as shown in Figure 4(b). The microphotograph of the photonic chip is shown in Figure 4(c). The chip has an area of 1000 μm x 950 μm, while the emitter aperture area is 77 μm x 77 μm. The chip was fabricated at Institute of Microelectronics (IME) using their 180 nm silicon-on-insulator (SOI) photonic process.

Figures 4(a)-4(c) show the structure of different photonic devices used in the implementation of the proposed OPA. Figure 4(a) shows the 200-μm long thermal phase shifter, which consists of a metal heater on top of a silicon waveguide and two thermally isolating deep trenches on the sides to enhance the thermal efficiency. The phase shifter has a measured resistance of 350 Ω and an I_π of 4.5 mA.

Figure 4(b) shows the structure of a grating coupler (serving as the OPA element) along with the corresponding row and column waveguides and the feed network. The IME 180 nm SOI process offers three silicon etch levels that are used in the design of the compact directional couplers, grating couplers, and the compact waveguide crossings. Directional couplers with varying lengths are used in order to equally distribute the optical power in each row and column. To make the element spacing as small as possible, the coupling lengths should be minimized, which is achieved by partially etching the gap in the coupling region to increase the coupling coefficient for a given length. The coupling lengths and the etch depth for the 7 directional couplers in each row/column are simulated to determine the transmission and coupling coefficients of the directional couplers and to predict the loss of the waveguide crossings. Note that the 500-nm wide 220-nm thick single-mode nanophotonic waveguides have a measured loss of under 2 dB/cm.

In the design of the grating couplers, which serve as the OPA emitters, the device dimensions and the number of grating "teeth" are modified to optimize the coupling efficiency for a compact footprint. The simulated efficiency of the grating coupler is about 30% at 1500 nm. To further reduce the element spacing, a compact waveguide crossing structure is designed that has a simulated insertion loss of under 0.3 dB with an isolation of more than 30 dB. To achieve symmetric routing, the grating couplers are placed at a 45 degree angle with respect to the column waveguides.

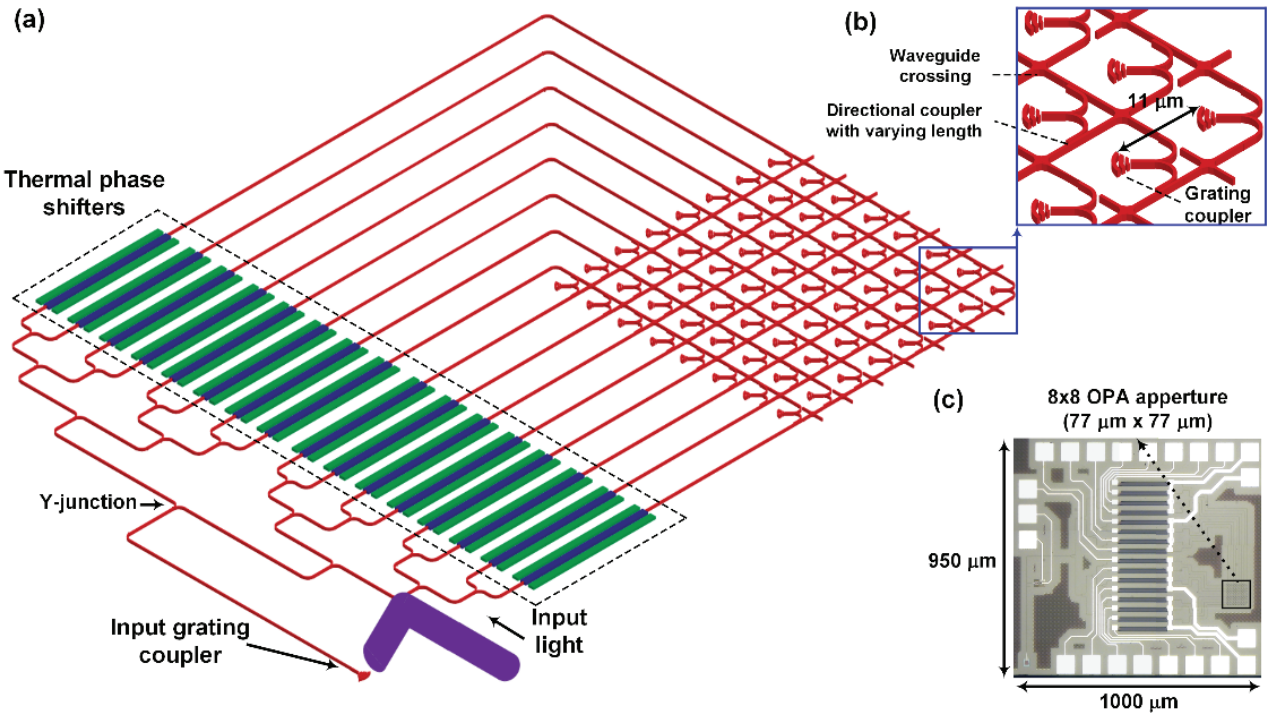

Figure 4: The Structure of Different Photonic Devices Used in the Implementation of the Proposed OPA

The structure of the implemented 8x8 OPA with 16 phase shifters placed outside of the array aperture (a). The structures of the grating couplers (as OPA elements) and directional couplers with varying lengths (b). The microphotograph of the implemented 8x8 OPA chip fabricated in IME's 180 nm SOI process (c).

3.3 Multi-layer OPA

To implement a multi-layer OPA, a commercial silicon photonic process that features two vertically-stacked layers of photonic devices in silicon (Si) and silicon nitride (SiN) was used. Figure 5(a) shows Si and a SiN nanophotonic waveguides and the fundamental optical mode in each waveguide when separately excited at 1550 nm.

Figure 5(b) shows the structure of a vertically-aligned tilted antenna, formed by stacking grating structures (scatterers) tilted by 45° with respect to the central axis of the feed waveguides (dashed lines) implemented on Si and SiN layers. This is to align the optical waves emitted from perpendicular Si and SiN waveguides serving as antenna feed lines. The green arrow shows the direction of radiation. Each tilted grating tooth can be viewed as an N-segment sub-wavelength structure that scatters the optical wave traveling in each feed waveguide (Figure 5(c)). Since the grating tooth is titled by 45° with respect to the feed waveguide axis, the optical wave traveling in the feed waveguide arrives at different segments of a grating tooth at different time resulting in the scattered light from each segment of a tooth to have a different optical phase. Consider the case when waves scattered from adjacent segments of a grating tooth to have a relative phase of $\Delta\phi$. In this case, this relative phase can be calculated as

$$\Delta\phi = \beta\Delta x = \left(2\pi n / \lambda_0\right)\Delta x, \tag{1}$$

where $\beta, n, \lambda_0, d = \sqrt{2}\Delta x$, and Δx are the wave propagation constant along the waveguide axis (i.e. x-axis), index of refraction of the waveguide medium, the wavelength of the light in free space, the segment pitch and the segment pitch projected on the waveguide axis, respectively. In this case, a grating tooth can be modelled as an N-element 1-D phased array for which the array factor (AF) can be written as

$$AF = \sum_{n=1}^{N} e^{j(n-1)\psi}, \tag{2}$$

where $\psi = \beta d \cos\varphi + \Delta\phi$ and φ is the azimuthal angle of radiation, which for a grating tooth parallel to the y-axis, is 0°. The magnitude of the array factor in Eq. (2) can be written as

$$\left|AF\right| = \frac{\sin\left(\frac{N}{2}\psi\right)}{\sin\left(\frac{1}{2}\psi\right)}. \tag{3}$$

The maximum of Eq. (3) occurs for $\psi = 2m\pi$, where m is an integer number. Therefore, the azimuthal angle of radiation can be calculated as

$$\varphi = \cos^{-1}\left(\frac{\lambda_0\Delta\phi}{2\pi nd}\right) = 45^{\circ}. \tag{4}$$

Hence, by tilting the grating teeth, the azimuthal angle of radiation can be changed and, by carefully designing the grating structures on Si and SiN feed waveguides, the emitted optical waves from vertically-stacked grating antennas can be aligned. Note: given the difference between the refractive indices of Si and SiN, the grating periods must be designed to ensure the same angle of emission from the stacked antennas. At a given wavelength, the polar angle of radiation with respect to the z-axis (normal to the feed waveguides) is written as $\theta = \sin^{-1}\left(\frac{n_w}{n_0} - \frac{\lambda_0}{\Lambda}\right)$, where n_w, n_0, and Λ are the refractive index of the waveguide medium (Si or SiN), the refractive index of the cladding (SiO_2), and the grating period, respectively. Therefore, the larger index of refraction of Si necessitates smaller grating period for the Si antenna. The simulated far-field pattern of the stacked grating antennas in Figure 5(b) is shown in Figure 5(d), where an azimuthal angle of radiation of 45° with respect to the central axis of feed waveguides is observed.

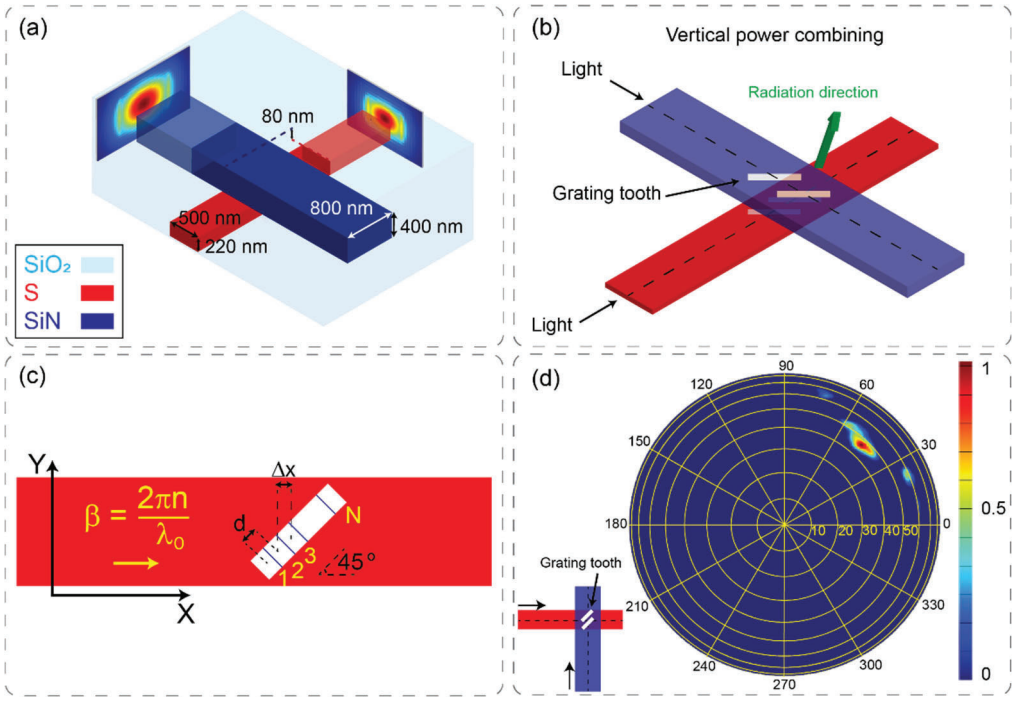

Figure 5: Tilted Grating Structures to Implement Vertically-stacked Optical Antennas
(a) Two single-mode waveguides in Si and SiN layers and the corresponding dimensions and optical mode profiles. The layers have a vertical spacing of 80 nm. (b) An optical antenna composed of two vertically-aligned tilted grating structures on Si and SiN waveguides. The gratings are 45° tilted with respect to the corresponding waveguide axis (dashed lines). (c) Structure of a multimode waveguide with a tilted grating structure which consists of N sub-wavelength scatterer segments and can be modelled as a 1-D phased array. (d) Simulated far-field interference pattern of a tilted vertically-aligned optical antenna shown in Figure 1(c) in which an azimuthal angle of 45° with respect to the waveguide axis can be seen.

Figure 6(a) shows an array of vertically-stacked tilted grating antennas formed in Si and SiN layers used to simulate beam forming. Within the near field of each vertically stacked grating antenna, the light emitted from the bottom tilted grating antenna (implemented on Si) is vertically combined with the light emitted from the top tilted grating antenna (implemented in SiN). To reduce the antenna pitch, tilted grating antennas are implemented on multimode feed waveguides for both bottom and top layers. To ensure equal emitted power from the grating antennas on each feed waveguide, the length of the grating antennas is gradually increased while the grating period is kept constant (Figure 6(a)). Note that if the aspect ratio of a grating tooth approaches unity (corresponding to a square grating tooth), the far-field pattern of the grating antenna would be symmetric ($\varphi \approx 0$).

The schematic of a 4x4 OPA formed using two vertically aligned 4x4 arrays on Si and SiN layers with an element-spacing of 3 μm. Grating lengths increase as the light propagates in the feed waveguide to achieve uniform optical power distribution (a). Simulated far-field interference pattern of the OPA (b). Conceptual schematic of an NxN OPA with 2N off-aperture phase shifters (c).

The electric fields at the input of the m[th] row and nth column have the same amplitude of a_0 and phases of ϕ_m, θ_n, respectively, resulting in a phase of $(\phi_m + \theta_n)/2$ for the element at the intersection of the two waveguides. To perform 2-D steering of a single optical beam, the relative phase between the adjacent elements in rows and columns can be set to $\Delta\phi_{m+1,m,n} = \Delta\phi$ and $\Delta\theta_{m,n+1,n} = \Delta\theta$, respectively. (d) Simulated 2-D beam-steering using the 4x4 OPA.

This sets the minimum achievable length of the first grating antenna on the feed waveguide given the grating period. Therefore, in designing the grating structures, the aspect ratios are carefully chosen to ensure the desired radiation angle. Linear waveguide tapers are used between single-mode routing waveguides and multimode feed waveguides. To verify the beam-forming performance of OPAs with vertically stacked tilted grating antennas, the far-field pattern for an array of 4x4 of such antennas is simulated, which is shown in Figure 6(b).

In order to lower the photonic routing complexity to allow for more closely spaced elements, off-aperture phase adjustment of the rows and columns of the phased array is utilized. For an NxN OPA, N phase shifters can be used outside the OPA aperture to set the relative phase between N rows of Si feed waveguides.

Similarly N off-aperture phase shifters can be used to set the relative phase between N columns of SiN feed waveguides. In such a remote phase adjustment method, as shown in Figure 6(c), the required relative phase between the elements for 2-D beam-steering can be set by properly setting the row and column phases. This approach significantly reduces the photonic and electrical routing complexities as well as the power consumption and the metallic-induced optical loss within the aperture. Figure 6(d) shows the simulated beam steering for the array of 4x4 vertically stacked tilted grating antennas shown in Figure 6(a).

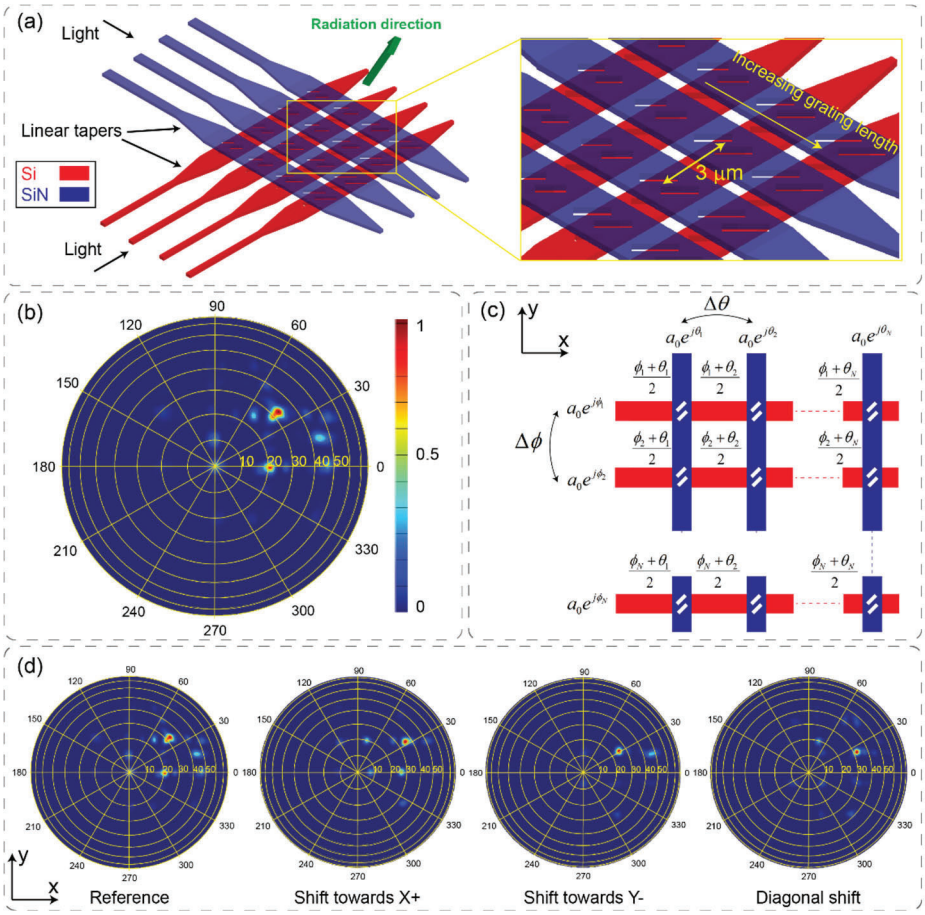

Figure 6: Simulated Beam Steering using an OPA with Vertically Stacked Grating Structures

Figure 7(a) shows the structure of the implemented 8x8 multi-layer OPA chip with two vertically stacked device layers of Si and SiN with a vertical spacing of 80 nm. Since Si offers a higher optical confinement (in conjunction with a SiO_2 cladding) due to its larger refractive index compared to SiN, it is the preferred layer to use for optical routing as it supports structures with higher densities.

The input light is coupled to the chip using a grating coupler implemented in the Si layer and is then split into 16 branches using 4 layers of Y-junctions, resulting in 8 row signals and 8 column signals. Within each row/column waveguide, the phase of optical wave is adjusted using a thermal phase shifter. The phase-adjusted signals are routed to two vertically stacked 8x8 arrays of waveguide grating structures; one in Si (red, rows) and one in SiN (blue, columns) as shown in Fig 7(b). The transition of light between Si waveguides and SiN waveguides takes place through vertical evanescent coupling. Tilted grating structures with a 3-μm pitch are designed as the OPA antenna elements by partially and fully etching the Si and SiN multimode waveguides, respectively. By setting the phase of the row elements in Si and column elements in SiN, the optical beam can be steered along X and Y directions, respectively. Note that the grating structures are placed at 45° with respect to the axis of the feed waveguides to align and vertically combine the optical waves emitted from the stacked grating structures within each antenna

element. The microphotograph of the OPA chip fabricated by Tower Semiconductor's 180-nm photonic process is shown in Fig. 7(c). Figure 7(d) shows the grating structure dimensions that are designed to ensure uniform power distribution. The average dimensions of the antennas is 1.5 µm x 2 µm.

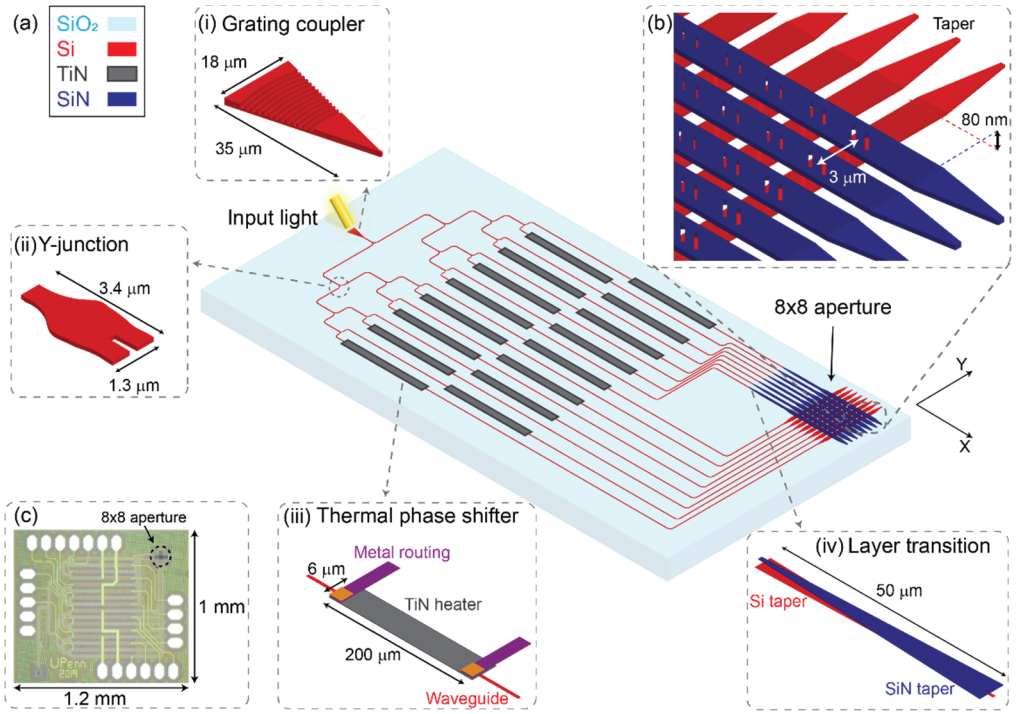

(d)

	1	2	3	4	5	6	7	8
Si: Length/width (µm)	0.8/0.2	1/0.2	0.8/0.2	1.2/0.2	1.1/0.25	1.5/0.25	1.5/0.2	1.7/0.25
SiN: Length/width (µm)	0.7/0.2	1/0.2	1.2/0.2	1.3/0.2	1.5/0.2	1.8/0.2	1.8/0.35	2/0.55

Figure 7: Implemented 8x8 Compact Multi-layer OPA

(a) The schematic of the proposed OPA implemented on Si and SiN device layers is shown. The input light is coupled into the chip using a grating coupler (i) and is split into 16 signals using Y-junctions (ii). The thermal phase shifter shown in (iii) consists of a TiN metal heater placed on top of a Si waveguide. The photonic layer transition (iv) consists of two vertically-stacked Si and SiN waveguide tapers. (b) Zoomed-in view of the OPA multi-layer aperture showing the grating structures in Si (partially etched) and SiN (fully-etched) vertically-stacked with 80-nm spacing to combine the row and column signals. (c) The microphotograph of the OPA chip fabricated by Tower Semiconductor's 180-nm silicon photonic process. (d) The width and length of the grating structures implemented in Si and SiN layers used to construct the antenna elements of the implemented 8x8 OPA.

3.4 Multi-Layer OPA Structure

In this multi-layer OPA architecture, an array of doped silicon pillars are placed on an optical distribution network. Each silicon pillar acts as a vertical phase shifter. Figure 8(a) shows the structure of this OPA. The input light is coupled to the SiPh chip and is divided to many rows using layers of Y-junction splitters. Here only four rows are shown to ease the illustration. An

optical phase modulator (*e.g.* thermo-optic modulator) is placed on each row waveguide. Each row waveguide is then tapered to a multi-mode waveguide. On each multi-mode waveguide, grating structures are placed to vertically couple the light into the pillar array. The width of the grating structures is gradually varied to ensure that equal power is coupled into each pillar. Conductor lines connect the top side of the column of pillars. The other side of each pillar is considered as the ground. In this case, the relative phase between the rows of the pillars is set using the on-chip phase modulators and the relative phase between the columns of the pillars is adjusted the pillar currents flowing from the top conductor to ground. In this case, 2-D beam-steering can be achieved. As shown in Figure 8(b), thin layers of Indium-Tin-Oxide (ITO) can be used as the top conductor while introducing negligible optical loss.

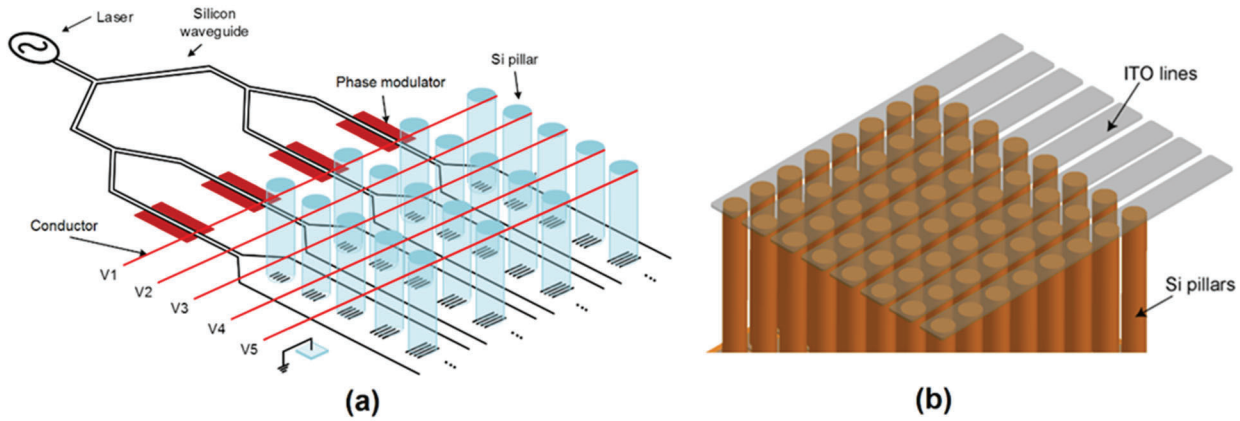

Figure 8: Structure of the OPA with Silicon Pillars as Vertical Optical Phase Shifters

3.5 Optical Distribution Chips

Figure 9(a) shows the distribution network, where an array of 8x8 ultra-compact grating couplers, were designed and taped-out. The array is composed of parallel silicon-on-insulator waveguides (referred to as bus waveguide). In each bus waveguide, the width is tapered from 500 nm to 1.2 μm.

Compact grating couplers with varying sizes are fabricated on each bus waveguide. The width of the grating couplers gradually increases to ensure equal power is emitted from all grating couplers. An array of fabricated silicon pillars will be placed on top of the grating coupler array. Figure 9(d) shows the measured emitted power from each grating coupler on a single waveguide bus showing a high power distribution uniformity.

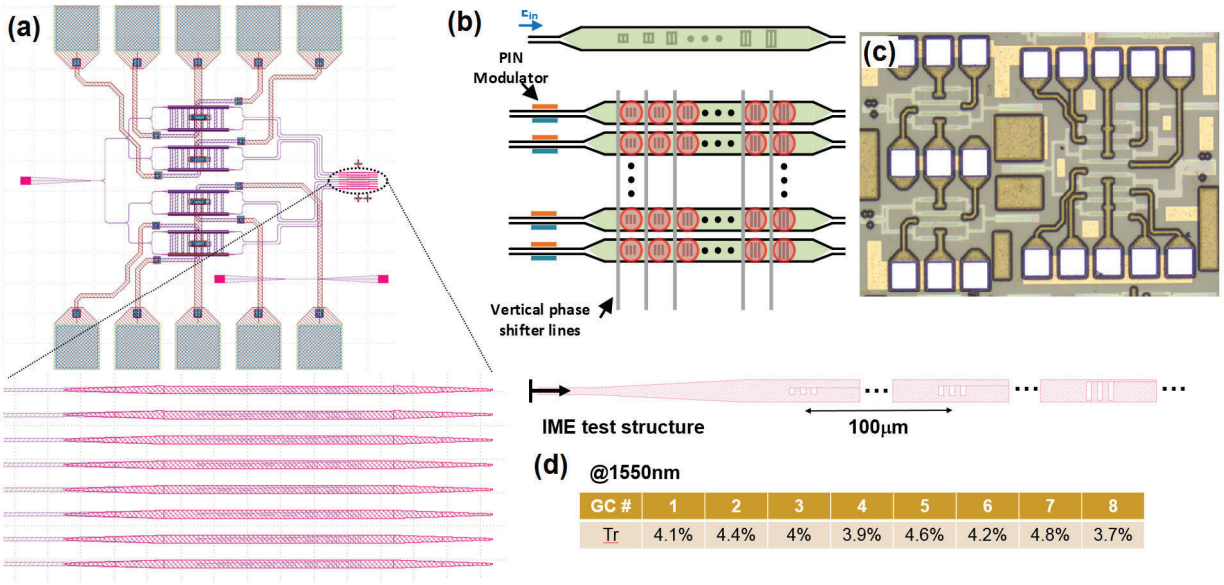

GC #	1	2	3	4	5	6	7	8
Tr	4.1%	4.4%	4%	3.9%	4.6%	4.2%	4.8%	3.7%

Figure 9: The Fabricated Photonic Chip with an Array of 8x8 Grating Couplers
The PIN modulators placed on each row as the base for the pillar array (a). The structure of the parallel with grating structures (b). The chip microphotograph (c). A separately fabricated waveguide with grating structures and the measured emitted power uniformity from the grating structures (d).

3.6 Multi-Layer OPA Fabrication Steps

A thin layer of SiNx is deposited on a carrier wafer acting as an etch-stop layer. A doped Si wafer is bonded and polished/etched to be as thick as 30 μm (step 2). Then Si pillars are patterned and etched (step 3). The gaps between the pillars have to be filled and planarized after the etch-back process to run conductive electrodes and make contact to the pillars (step 4). In step 5, a thin layer of SiO_2 is deposited and patterned. ITO traces are patterned and deposited acting as a transparent conductive electrodes followed by metal deposition for pads and traces (steps 6 and 7). The backside of the chip is etched to create an opening (steps 8 and 9). The ITO layer is deposited as a common ground layer which connects all pillars together (step 10). The fabricated chip is finally transferred on the taped-out silicon photonics chip (step 11).

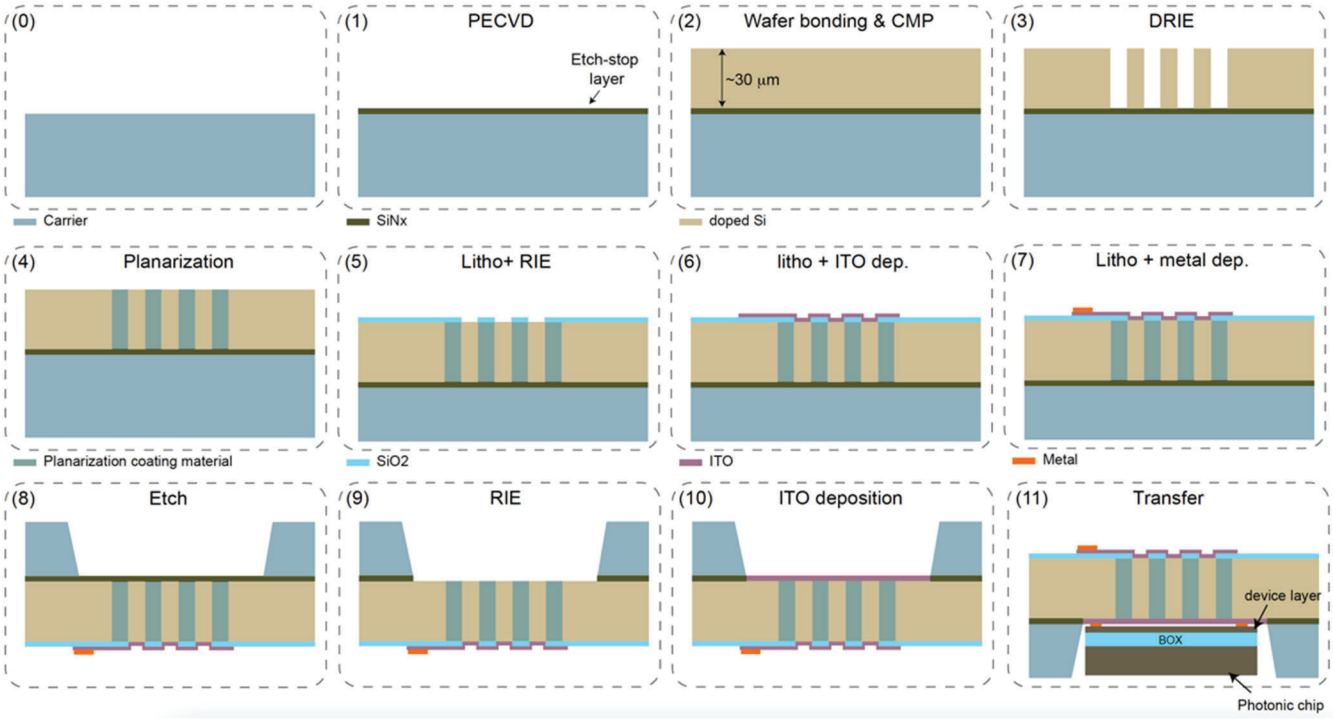

Figure 10: Illustrates the Fabrication Steps of the Proposed OPA

Figure 11(a) to 11(d) shows the fabricated 28-μm tall pillar test structures with element diameter/spacing of 3μm/1μm, 1μm/1μm, 0.8μm/1.2μm, and 2μm/2μm, respectively. Using the outcome of the design and fabrication of these test structures, a highly uniform array of 32x32 silicon pillars with element diameter/spacing of 1.2μm/0.8μm has been fabricated which is shown in Fig. 11(e). Figure 11(f) shows the fabricated 15-μm tall 64x64 silicon pillar array.

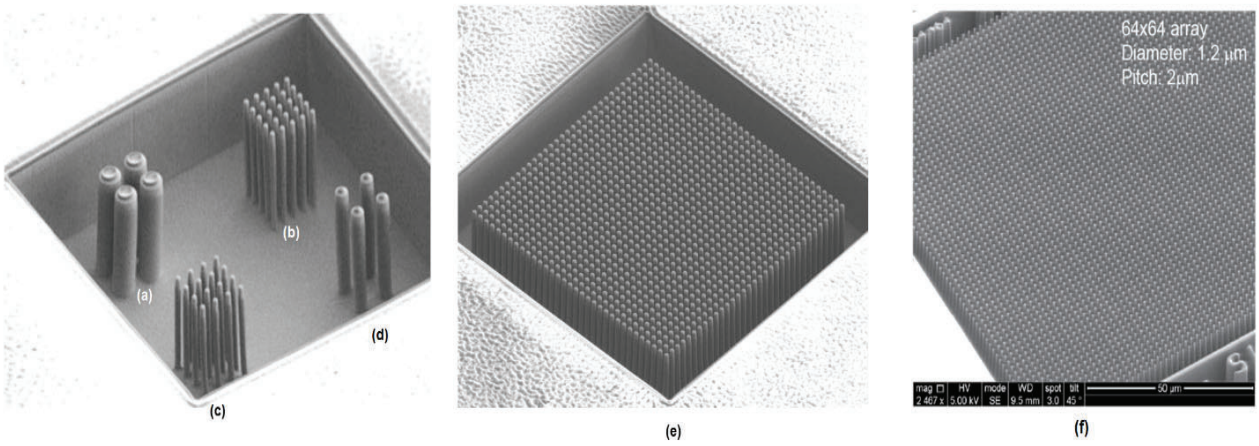

Figure 11: Fabricated Pillar Arrays

Figure 12 shows the fabrication steps for metallization of a 32x32 pillar array. A thick layer of SiO_2 was deposited on the Si pillars (step 1). As shown in step 2, ITO lines are patterned, and a 100-nm thick ITO film is sputtered using a PVD process. One of the important parameters in this step is the line resolution as well as the overlay accuracy using the direct laser write

lithography. Finally, electrodes are patterned, and a layer of 100-nm thick Au is deposited to connect the ITO lines to the pads. Figure 12 (right) shows the microphotograph of the final device.

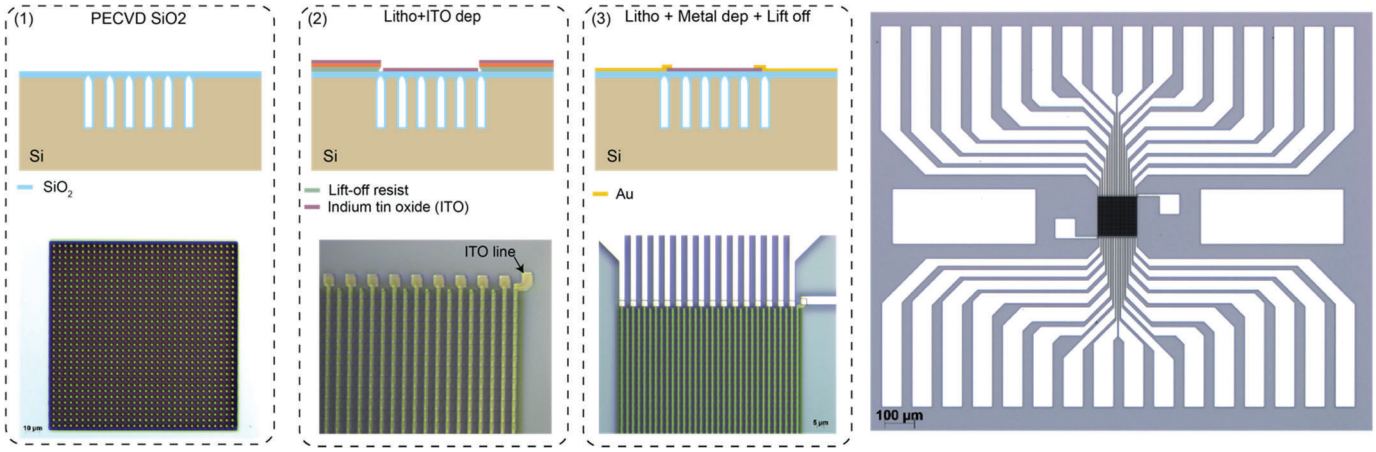

Figure 12: Fabrication Steps for Metallization of a Pillar Array

4 RESULTS AND DISCUSSION

4.1 Single Layer OPA

The measurement setup for characterizing the proposed OPA is shown in Fig. 13(a), where a laser emitting 1 mW at 1502 nm is coupled into the chip input grating coupler using a single-mode optical fiber. Two digitally controlled 8-channel thermal phase modulator drivers were used to control the row and column phase shifters. A FIND-R-Scope 85700A infrared camera with adjustable optics was used to monitor the far-field interference pattern of the OPA.

In order to demonstrate 2-D beam-steering, the thermal phase shifters are used to control the phase of the optical signals in each row and column. To account for the different waveguide routing lengths and process variations, the OPA was first calibrated, where the far-field interference pattern is compared with the simulation result for the case that both row and column signals have zero phase offset. Then, by adjusting the currents of the thermal phase shifters around the corresponding calibration point, 2-D beam-forming was demonstrated. Figure 13(b) shows four grating lobes in the far-field interference pattern of the OPA, which appear due to the $> \lambda/2$ emitter-to-emitter spacing. Figure 13(c) shows the 2-D beam-steering results (only one grating lobe is shown). By controlling the phase of the thermal phase modulators in the rows and columns, beam-steering range of about 7° is demonstrated. The corresponding beam profiles are shown in the bottom section of Figure 13(d) while the expected power consumption is depicted in Figure 13(e).

Please note that the estimated output power for each element grating coupler (emitter) is about 38 dB lower than the input laser power (coupled into the chip input grating coupler). This includes about 5 dB loss of the chip input grating coupler, ~2 dB excess loss of 4 layers of Y-junctions, ~1 dB loss of each modulator, distribution of input light among 64 elements corresponding to 18 dB split ratio, and about ~12 dB loss of each emitting structure (including about 30% emitting grating coupler efficiency). Also, for the case that the optical power coupled into the chip is set to -2 dBm, the measured radiated power in the main lobe is about -45 dBm. Note that given the fact that only 2N phase shifters are needed for N2-element OPA, the power consumption is reduced significantly. Figure 13(d) compares the simulated peak power consumption of a conventional N2-element OPA with that of an N2 OPA with remote phase adjustment implemented in this work. As an example, for a 1024x1024-element OPA, the peak power consumption of 9.4kW for a conventional OPA is reduced to 18.4W for an OPA with remote phase adjustment.

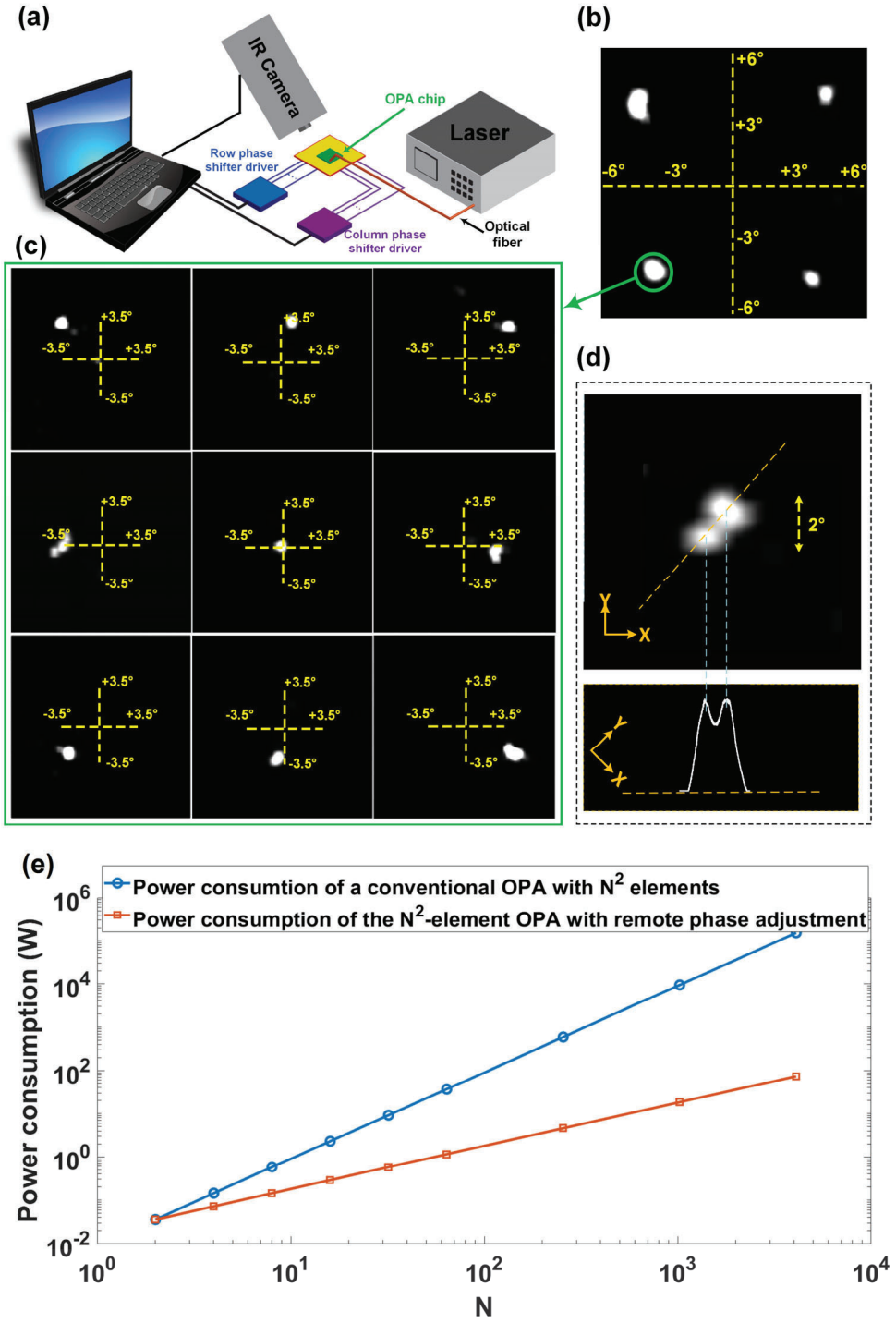

Figure 13: The Measurement Setup for Characterizing the Proposed OPA

Measurement setup used to characterize the OPA chip (a). Measured far-field interference pattern showing four grating lobes (b). Demonstration of the 2-D far-field beam-steering (c). Two consecutive resolvable spots while diagonal beam-steering is performed (d). The bottom portion of this figure shows the beam profiles. Power consumption projections comparing our approach with that of a conventional OPA (e).

4.2 Multi-layer OPA

The implemented OPA is characterized using the measurement setup shown in Figure 14(a). The wavelength of 1470 nm is chosen to have the best alignment between the optical waves emitted from the Si and SiN tilted grating antennas. An array of digitally controlled phase shifter drivers are used to control the relative phase between rows of Si feed waveguides. Similarly, the relative phase between columns of SiN feed waveguides is adjusted. The far-field interference pattern of the multi-layer OPA is monitored using an infrared camera.

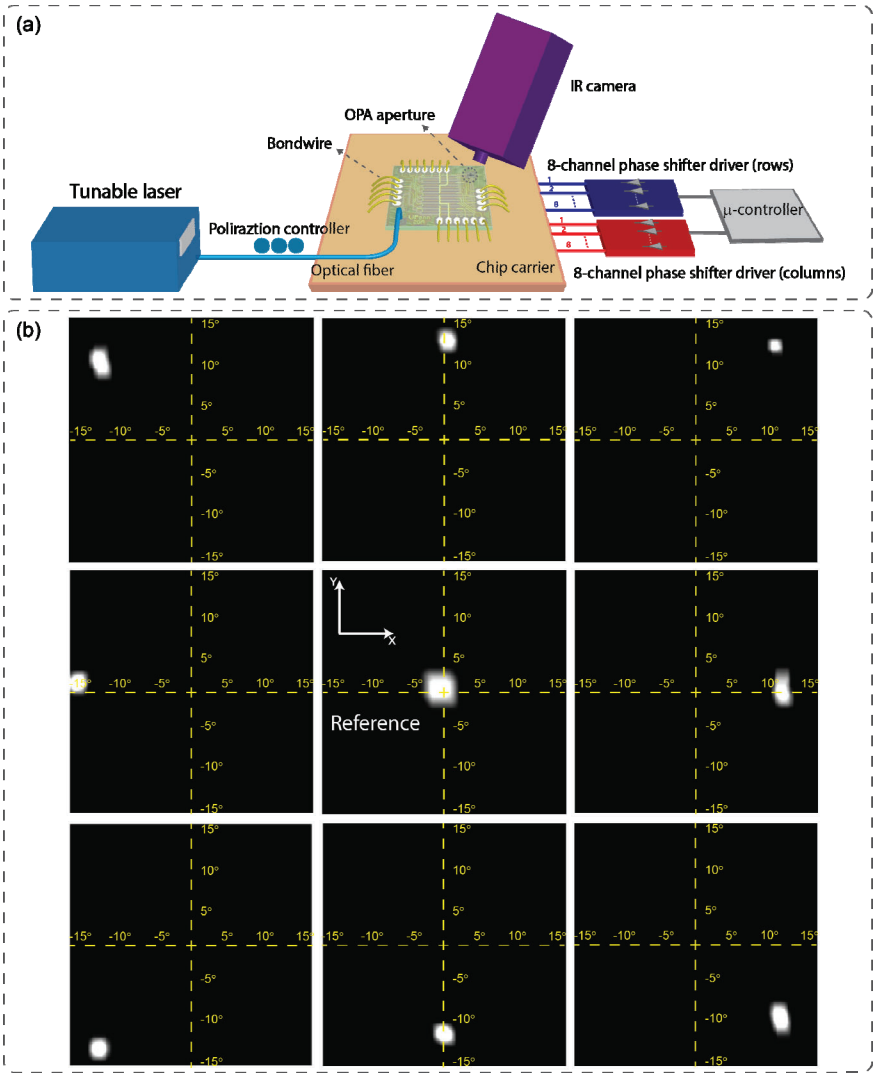

Figure 14: 2-D Beam-steering Demonstration

The measurement setup (a). The -3 dBm input light at 1470 nm is coupled into the chip using an optical fiber and after polarization adjustment. Two 8-channel phase shifter drivers, with an 8-bit per channel resolution are used. A microcontroller writes the proper digital control signals to the drivers. The far-field interference pattern is monitored using a FIND-R-Scope 85700A IR camera. (b) 2-D beam-steering results demonstrated using the implemented multi-layer OPA chip. A beam-steering range of about 23° is achieved.

Prior to the beam-steering demonstration, the OPA was calibrated to account for different waveguide lengths and process variations causing phase mismatch between antenna elements. After calibration, 2-D beam-steering is demonstrated (Figure 14(b)). The measured beam-steering range is about 23°. In addition, we observe the best beam alignment within about 4-nm bandwidth around the center wavelength of 1470 nm resulting in about 0.5 THz available bandwidth for free-space communication.

4.3 Passive Beam Forming and Steering

In order to do a proof-of-concept measurement, a passive free-space optical experiment is conducted where a pillar array is illuminated from its backside and an interference pattern is measured with the IR camera in the far-field. Figure 15(a) illustrates the experiment, where the optical signal is coupled into pillars with an incident angle of θ. Since silicon pillars are linearly spaced and the wave is illuminated at an angle, there is a time delay (or phase difference) between elements. This phase shift is a function of the wave number (inversely proportional to the wavelength). Figure 15(b) shows the measurement setup. Figure 15(c) compares the simulation and measurement of the far-field pattern for a 64x64 array (diameter 2 μm, spacing 2 μm) as a function of the laser wavelength. This measurement shows that the optical signal can be coupled into silicon pillars and the far-field interference pattern can be steered by adjusting relative phase between the emitters.

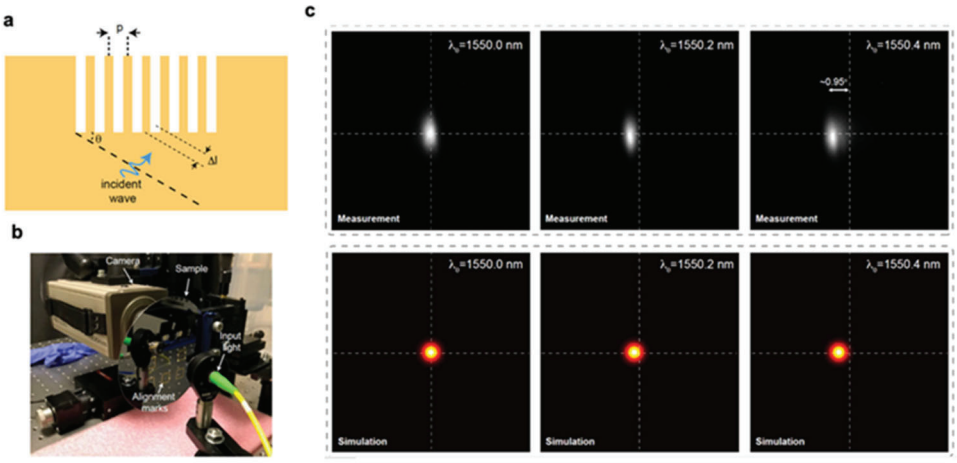

Figure 15: Beam-forming and Steering

4.4 Metallization and ITO Characterization

To perform 2-D beam steering, pillars have to be electrically connected in a row (column). If a highly conductive metal, such as Au, is used to metallize the pillars, the metal overlap with optical mode needs to be minimized to avoid optical loss and field distortion while maintaining electrical contact. This implies fabrication challenges when overlay accuracy is in the order of or less than the feature size. We used Indium-Tin-Oxide (ITO) as an optically transparent and electrically conductive film to create the electrical connection to the pillars. Figure 16 shows the optical and electrical characterization of 100-nm thick deposited ITO (In_2O_3/SnO_2, 90%:10%).

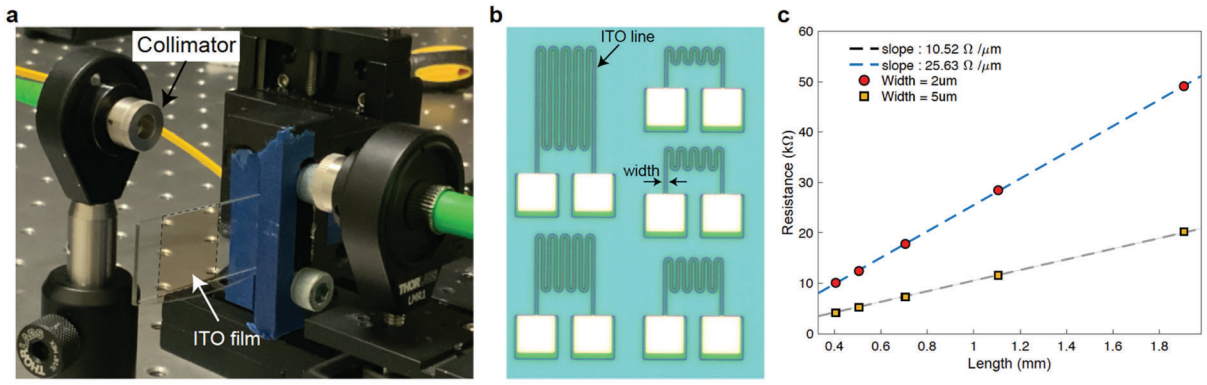

Figure 16: The Optical Characterization Setup for the ITO Film (a), the Fabricated ITO Lines for Electrical Characterization (b) and (c) Impedance Characterization of the Deposited ITO Film

Figure 16(a) shows the free-space optical measurement setup for insertion loss characterization. The 100-nm thick ITO film has about 1.5 dB of optical insertion loss at the wavelength of 1550 nm. Figure 16(b) shows the fabricated ITO resistors for sheet resistance characterization. As shown in Figure 16(c), the deposited ITO film has a sheet resistance of under 50 Ω per square.

5 CONCLUSIONS

In method 1, first, a novel architecture to perform 2-D beam-steering in an NxN OPA with only 2N phase shifters placed outside of the array aperture was demonstrated. In this case, the number of the phase shifters is reduced by a factor of N/2, which results in a significant power consumption reduction for a 2-D OPA with a large number of elements. As a proof of concept, an 8x8 OPA with 16 phase shifters outside of the aperture has been implemented and used to demonstrate robust 2-D beam-steering over a range of about 7°. Then, another novel structure for method 1 was designed and implemented, where a multi-layer single-wavelength OPA that benefits from 3-D light distribution and processing with off-aperture phase adjustment has been utilized. As a proof of concept, an 8x8 OPA was implemented in a commercial silicon photonic process that features two photonic device layers, i.e. Si and SiN, with only 16 off-aperture phase shifters and an element-spacing of 3 μm was achieved. We did meet and exceed the defined goals of the program using the architecture of the multi-layer OPA.

In method 2, we successfully and robustly fabricated many silicon pillar arrays, performed planarization, ITO and gold deposition and prepared the samples for transfer. Using the prepared samples, passive 1-D beam-steering has been demonstrated. Several optical distribution networks using different technologies have also been taped-out and characterized. However, due to the lab and clean room shutdowns due to Covid-19, we have not been to transfer the samples on the fabricated chips to date.

6 RECOMMENDATIONS

For method 1, scalability to multi-layer OPAs with a large number of emitters is possible and should be considered. The high element pitch enables true 2-D beam steering over a large field-of-view which may enable important applications ranging from LiDAR to free-space optical communication.

For method 2, the implementation of OPAs with sub-wavelength pitches and a large number of elements is feasible allowing for even a larger steering range. The per-element phase control offered by this architecture allows for the formation of sophisticated phase fronts which may prove useful e.g. to mitigate the effects of propagation through turbulent media.

7 REFERENCES

1 S. J. Spector, B. F. Lane, M. R. Watts, L. D. Benney, J. G. Delva, A. E. Hare, A. F. Kelsey, J. M. Mlynarczyk, E. S. Hosseini, C. V. Poulton, and J. P. Laine, "Broadband Imaging and Wireless Communication with an Optical Phased Array," in *Conference on Lasers and Electro-Optics*, OSA Technical Digest (online) (Optical Society of America, 2018), paper SM3I.7

2 W. Xie, T. Komljenovic, J. Huang, M. Tran, M. Davenport, A. Torres, P. Pintus, and J. Bowers, "Heterogeneous silicon photonics sensing for autonomous cars [Invited]," Opt. Express **27**, 3642-3663 (2019).

3 J. Sun, E. Timordugan, A. Yaacobi, E. Shah Hosseini, and M. R. Watts, "Large-scale nanophotonic phased array", Nature **493**, 195-199 (2013).

4 C. V. Poulton, *M. J. Byrd, P. Russo*, E. Timordugan, M. Khandaker, D. Vermeulen, and M. R. Watts, "Long-Range LiDAR and Free-Space Data Communication With High-Performance Optical Phased Arrays," in *IEEE Journal of Selected Topics in Quantum Electronics*, **25**, 1-8 (2019).

5 F. Aflatouni, B. Abiri, A. Rekhi, and A. Hajimiri, "Nanophotonic projection system," Opt. Express **23**, 21012-21022 (2015).

6 F. Aflatouni, B. Abiri, A. Rekhi, and A. Hajimiri, "Nanophotonic coherent imager," Opt. Express **23**, 5117-5125 (2015).

7 B. Abiri, F. Aflatouni, A. Rekhi, and A. Hajimiri, "Electronic Two-Dimensional Beam Steering for Integrated Optical Phased Arrays," in *Optical Fiber Communication Conference*, OSA Technical Digest (online) (Optical Society of America, 2014), paper M2K.7.

8 R. Fatemi, B. Abiri, and A. Hajimiri, "An 8×8 Heterodyne Lens-less OPA Camera," in *Conference on Lasers and Electro-Optics*, OSA Technical Digest (online) (Optical Society of America, 2017), paper JW2A.9.

9 S. Chung, H. Abediasl, and H. Hashemi, "15.4 A 1024-element scalable optical phased array in 0.18μm SOI CMOS," *2017 IEEE International Solid-State Circuits Conference (ISSCC)*, San Francisco.

10 C. V. Poulton, P. Russo, E. Timurdogan, M. Whitson, M. J. Byrd, E. Hosseini, B. Moss, Z. Su, D. Vermeulen, and M. R. Watts, "High-Performance Integrated Optical Phased Arrays for Chip-Scale Beam Steering and LiDAR," in *Conference on Lasers and Electro-Optics*, OSA Technical Digest (online) (Optical Society of America, 2018), paper ATu3R.2.

11 K. Van Acoleyen, H. Rogier, and R. Baets, "Two-dimensional optical phased array antenna on silicon-on-insulator," Opt. Express **18**, 13655-13660 (2010).

12 J. K. Doylend, M. J. R. Heck, J. T. Bovington, J. D. Peters, L. A. Coldren, and J. E. Bowers, "Two-dimensional free-space beam steering with an optical phased array on silicon-on-insulator," Opt. Express **19**, 21595-21604 (2011).

13 D. N. Hutchison, J. Sun, J. K. Doylend, R. Kumar, J. Heck, W. Kim, C. T. Phare, A. Feshali, and H. Rong, "High-resolution aliasing-free optical beam steering," Optica **3**, 887-890 (2016).

14 J. C. Hulme, J. K. Doylend, M. J. R. Heck, J. D. Peters, M. L. Davenport, J. T. Bovington, L. A. Coldren, and J. E. Bowers, "Fully integrated hybrid silicon two dimensional beam scanner," Opt. Express **23**, 5861-5874 (2015).

15 T. Komljenovic, R. Helkey, L. Coldren, and J. Bowers "Sparse aperiodic arrays for optical beam forming and LIDAR," Opt. Express **25**, 2511-2528 (2017).

LIST OF SYMBOLS, ABBREVIATIONS, AND ACRONYMS

ACRONYM	DESCRIPTION
1-D	One Dimensional
2-D	Two Dimensional
3-D	Three Dimensional
AFRL	Air Force Research Laboratory
DARPA	Defense Advanced Research Projects Agency
GC	Grating Coupler
IME	Institute of Microelectronics
ITO	Indium-Tin-Oxide
OPA	Optical Phase Array
PVD	Physical Vapor Deposition
SiN	Silicon Nitride
SiPh	Silicon Photonics
SOI	Silicon-on-Insulator
TSV	Through Silicon Via